# 1 Hybridized Orbital Ordering Project – Orbital hybridization ordering study in strongly correlated electron system and the external field effect –

*Project Leader: Hironori Nakao*

## 1-1 Introduction

Various intriguing physical properties have been discovered in strongly correlated electron systems (SCES). In such systems, the strong correlation among charge, spin, and orbital of the *3d* electrons and lattice degrees of freedom play important roles. Hence, it is important to study these electronic states in order to understand the phenomena microscopically. Moreover, marked properties, such as high $T_c$ superconductivity and colossal magnetoresistance effects, have been often reported near the metal-insulator (MI) transition, where the localized electrons, *d*-electrons in transition metals and *f*-electrons in rare earth metals, and the itinerant electrons, O*2p*, P*3p*, and so on, compete with each other. For example, superconductors generally exist in the vicinity of a quantum critical point. Hence, it is important to study the orbital hybridized states where itinerancy and localization of electrons compete in order to elucidate the origin of these physical properties. Recently, new types of ferroelectric (FE) compound such as multiferroic compounds have attracted much attention. There, the hybridized orbital is a key parameter of the polarization, and so the study of hybridized orbital states is important. In this project, the hybridized orbital states near the MI transition and in FE compounds were investigated by the complementary use of hard and soft X-rays. Especially, resonant soft X-ray scattering is an important technique to clarify these electronic states and the orbital hybridized states. The external field effect on orbital hybridized states is also an important subject in this project.

In general, the resonant signal reflecting the change of physical properties is quite weak, and so the X-ray detector used to detect the weak signal is a key technology. However, previously there was no good detector that could detect one photon and be used in a vacuum. We have therefore developed a silicon drift detector as shown in Fig. 1. By using this detector and the slit in a vacuum, the background fluorescence from the sample is remarkably reduced. This is crucial for resonant X-ray scattering experiments, since fluorescence is unavoidable in such experiments. Finally, we used this detector to investigate physical properties in SCES by the resonant soft X-ray scattering technique.

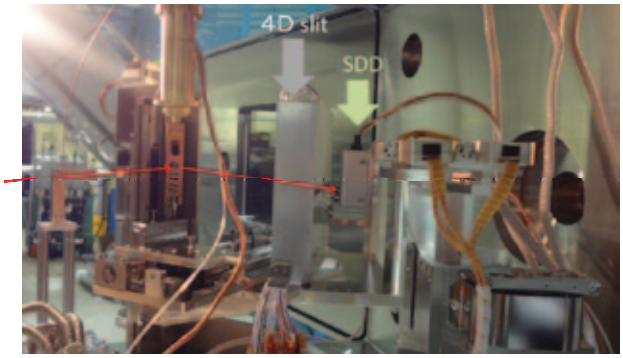


Fig. 1 Developed new silicon drift detector in the vacuum chamber. The red arrows indicate the incident and scattered X-rays.

Our research encompasses various subjects such as transition metal oxides, rare earth metal compounds, and organic conductors, which are typical systems in the SCES, and is being performed in collaboration with many external researchers. Here, we report recent studies of layered nickelate, $Nd_{2-x}Sr_xNiO_4$ [1], hollandite chromium oxide, $K_2Cr_8O_{16}$ [2,3], and a new ferroelectric compound, $Sr_{1-x}Ba_xMnO_3$ [4]. The orbital-spin orderings in $RVO_3$ studied by complementary use of neutrons and X-rays [5,6] are also reported.

## 1-2 Doping variation of hole orbital states in $Nd_{2-x}Sr_xNiO_4$ (0.3•x•1.1) as studied by polarization-dependent soft-X-ray absorption spectroscopy [1]

X-ray absorption spectroscopy (XAS) is a strong probe for determining local electronic structures such as the valence as well as the orbital states. In the case of superconducting layered cuprates, for example, a couple of pre-edge peaks have been clearly observed in the O *K*-edge spectra and the relationship between the orbital character and superconductivity has been intensively studied [7]. While XAS experiments have been performed also for layered nickelates for comparison with superconducting cuprates, previous works on single crystals were limited to the low-doping region below about x = 0.5 [8]. We are thus investigating the orbital state variation toward a metallic region by systematically measuring the polarization-dependent O *K*-edge spectra up to x = 1.1.

Single-crystalline samples of $Nd_{2-x}Sr_xNiO_4$ (x = 0.3–1.1) were grown by the high-oxygen-pressure floating-zone method. XAS experiments were carried out at undulator beamline BL-16A of the Photon Factory in KEK. The O *K*-edge data were taken in fluorescence-yield mode with a typical attenuation length of about 300 Å. The XAS spectra for E||*a* and E||*c* were measured using vertically and horizontally polarized X-rays in nearly-grazing incidence geometry to the *ab* plane, respectively, for comparing and

analyzing the polarized spectra more accurately. The incidence angle relative to the surface was set to 10°. The measurements were performed in a high vacuum of $10^{-8}$ torr, at 50 K.

Figure 2(a) shows the polarization-dependent O *K*-edge spectra at x = 0.5 for E||*a* and E||*c*. Aside from the main peak at about 536 eV, a couple of pre-edge peaks are clearly observed in the lower energy region (3 peaks for E||*a* and 2 peaks for E||*c*), as labeled with letters **A**-**D**. Considering all the possible transition processes as shown in Fig. 2(b), these pre-edge peaks at about 532 and 529 eV for x = 0.5 are ascribable to processes **A** and **B**, as assigned also in the previous work [8]. This simply indicates that the holes are mainly doped into the $x^2$-$y^2$ orbital below x = 0.5. Figures 2(c) and 2(d) show the doping variation of the magnified spectra in the pre-edge region. Focusing on the variation below and above x = 0.5 for E||*c*, an additional peak assigned to process **C** is clearly discerned above x = 0.6, directly indicating the existence of $Ni^{3+}$ sites with unoccupied $3z^2$-$r^2$ orbital. Above x = 1.0, in addition, the total peak positions largely shift to lower energy both for E||*a* and E||*c*. This might arise from the appearance of an additional peak assigned to process **D**, indicating the existence of $Ni^{4+}$ sites as the ground state.

Eventually, doping variation of the site occupancy of the respective valence and orbital states can be roughly estimated by fitting and quantifying the pre-edge peaks **B**-**D** for E||*c* [1]; the number of $Ni^{3+}$ sites with occupied $3z^2$-$r^2$ and $x^2$-$y^2$ orbitals increases nearly linearly at about x = 0–0.5 and x = 0.5–1.0, respectively. This indicates that the excess holes above x = 0.5 are mainly doped into the $3z^2$-$r^2$ orbital and thus the *x2-y2*-based checkerboard-type charge ordering or correlation can strongly persist up to the high-doping metallic region due to the multi orbital nature.

### 1-3 Structural study of ferromagnetic metal-insulator transition in hollandite chromium oxide, $K_2Cr_8O_{16}$ [2,3]

Ferromagnetic insulator (FI) is extremely rare in transition-metal oxides. Usually it is met in metallic systems and is caused by double exchange. Insulating ferromagnets are definitely not common among these materials. All the more surprising was the recent discovery [9] that chromium hollandite $K_2Cr_8O_{16}$ first becomes ferromagnetic at $T_c$ = 180 K and with decreasing temperature, it experiences a metal-insulator transition (MIT) at $T_{MI}$ = 95 K, remaining ferromagnetic at low temperature. $K_2Cr_8O_{16}$ are mixed valent oxides with $Cr^{3+}/Cr^{4+}$ = 1/3 (average valence of $Cr^{3.75+}$). In this study, we undertook a structural determination to elucidate this unique ferromagnetic MIT. The synchrotron X-ray diffraction experiment for the single crystal was performed at beamlines (BL) 8A and 8B of the Photon Factory in KEK.

We first confirmed that the structure of the ferromagnetic metallic (FM) phase is isomorphous to that in the paramagnetic metallic (PM) phase, where all the Cr sites are crystallographically equivalent. Next, the structural change at $T_{MI}$ was explored by the oscillation photographs. The superlattice reflections with $q$ = ($a^*$/2, $b^*$/2, $c^*$) were clearly observed at 20 K (< $T_{MI}$), indicating that the unit cell becomes $\sqrt{2}a$ x $\sqrt{2}b$ x $c$ in the FI phase, where $a$, $b$ and $c$ are the lattice parameters in the PM and FM phases (Fig. 3). The intensity of the superlattice reflections was $10^{-3}$ times weaker than that of the fundamental ones. Although peak splittings were not

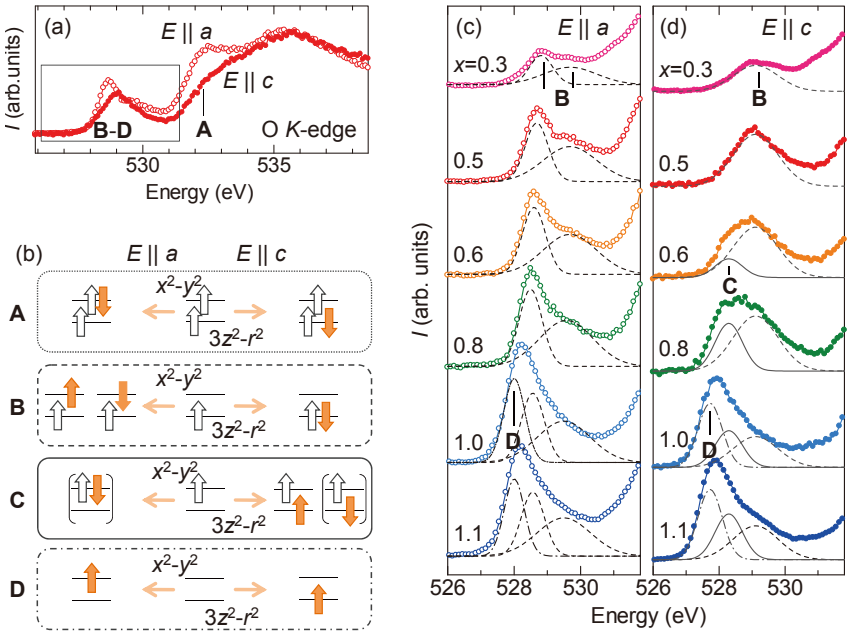


Fig. 2 (a) Polarization-dependent O *K*-edge XAS spectra. (b) Schematic of the transition processes **A**-**D** corresponding to the pre-edge peaks. Filled arrows represent the transition electrons from the O 1*s* state to the ground Ni 3*d* $e_g$ orbital state shown in the middle. Doping variation of the magnified O *K*-pre-edge spectra for (c) E||*a* and (d) E||*c*. Fittings for the peaks corresponding to the transition processes (**B**, **C**, and **D**) as labeled in (b) are indicated by dashed, solid, and chain curves, respectively.

observed, the equivalent/inequivalent superlattice reflections agree with the condition of the Laue class 2/*m*, which implies disappearance of the four-fold axis, indicating a monoclinic structure. Finally, we concluded that the space group of the FI phase is *P*1121/*a* from a detailed analysis of the reflection conditions. The transition is accompanied by symmetry breaking, with the losses of the four-fold axis and the mirror plane perpendicular to the *c* axis.

The structural analysis was performed taking the twinning structure which includes domains (*a*, *b*, *c*) and (*b*, -*a*, *c*). When the ratio of the twin volume fraction was 0.608(1) : 0.392, we obtained good reliability factors (R-factor = 0.025, $R_w$ = 0.085).

Figure 3 shows the resulting crystal structure of the FI phase. In the FI phase, four Cr sites, two K sites and eight O sites become crystallographically inequivalent in contrast to unique Cr and K sites and two O sites in the FM and PM phases. The four Cr sites form three kinds of double chains by sharing edges Cr1-Cr3, Cr2-Cr2 and Cr4-Cr4 octahedra, respectively. Three kinds of double chains are arranged such that the four Cr sites form a rectangular four-chain column by sharing corner oxygens.

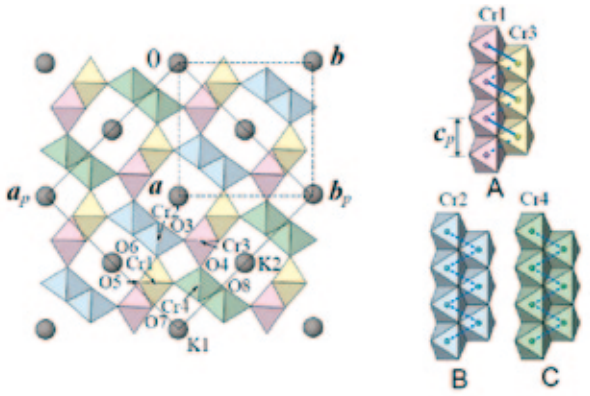


Fig. 3 (left) Crystal structure of the ferromagnetic insulator phase in $K_2Cr_8O_{16}$ viewed from the c-axis. (right) Three kinds of double chains. In the structure. there are four Cr sites (Cr1–Cr4).

At the same time, the four-chain column has Cr-O bond alternations. This structural distortion can be understood as the formation of tetramers of Cr ions in the *c*-direction in each of the four-chain columns; the lattice-dimerization occurs in four-chain columns, as shown in Fig. 4(b).

Such observed structural characteristics well coincide with a Peierls mechanism for the metal-insulator transition proposed from electronic structure calculations [2]; one extra electron is weakly localized in the tetramer of Cr1–Cr4 due to Peierls instability inherent in a one-dimensional electron system characterized by the rectangular four-chain column.

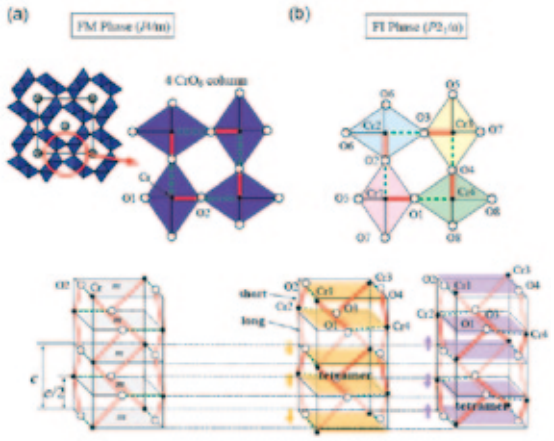


Fig. 4 (a) Schematic illustrations of the four-chain columns for (a) the FM phase and (b) the FI phase. In the FI phase, the four-chain columns have the Cr-O (Cr-Cr) bond alternations, indicating the lattice-dimerization with the formation of Cr-tetramers.

**1-4 Displacement-type ferroelectric transition with off-center magnetic $Mn^{4+}$ ions in perovskite $Sr_{1-x}Ba_xMnO_3$ [4]**

Since the discovery of ferroelectricity in perovskite $BaTiO_3$ in the 1940s, a variety of ferroelectric oxides have been extensively studied for electronic device engineering as well as academic interest. Most of the perovskite ferroelectrics $ABO_3$ so far identified, however, consist of non-magnetic *B* (transition metal) sites with no *d*-orbital electrons. Typical examples include $Pb(Zr,Ti)O_3$ and $KNbO_3$. This empirical rule for the ferroelectric perovskites has been a severe restriction in designing new multiferroic materials where magnetism and ferroelectricity coexist, because magnetic ordering in contrast requires the partial occupation of the *d* shell of the transition metal ions [10]. Recently, however, several first-principles calculations have predicted the possible ferroelectric ground state with large polarization (tens of μC/cm$^2$) for $AMnO_3$ (*A* = Ca, Sr, and Ba), accompanied by the magnetic $Mn^{4+}$ ion displacement due to strong Mn-O bond covalency [11]. In reality, cubic $SrMnO_3$ is a typical Mott insulator with G-type (staggered in all three directions) antiferromagnetism and to be paraelectric down to the lowest temperature. Although the ferroelectric instability was predicted to be promoted with increasing ionic radius of the *A* site ions, no ferroelectric transition was experimentally observed up to 20% Ba substitution for Sr. For a larger radius of the *A* site ion, the hexagonal polymorph becomes so stable that the cubic perovskite structure cannot be synthesized by the conventional solid-state reaction.

To overcome this problem, we have developed a two-step crystal growth technique, consisting of a

floating-zone method and high-pressure oxygen annealing (~6 GPa) [4]. This enabled the synthesis of single crystals with the perovskite structure up to 50% Ba substitution.

Figure 5(a) shows the dependence of lattice constant *a* on Ba concentration (*x*) for $Sr_{1-x}Ba_xMnO_3$ ($0 \le x \le 0.5$). As *x* increases from 0 to 0.4, the lattice constant at 300 K monotonically increases from 3.807 to 3.856 Å while maintaining the cubic symmetry. Around $x = 0.45$, the crystal structure changes from cubic to tetragonal, indicating ferroelectric distortion with an elongation of the *c*-axis. Figure 5(b) shows a magnetoelectric phase diagram for $Sr_{1-x}Ba_xMnO_3$ as a function of *x*. The ferroelectric transition temperatures $T_C$ were determined as the temperatures where the tetragonal distortion vanishes. The G-type antiferromagnetic phase is stable over the entire doping range ($0 \le x \le 0.5$), although the transition temperature $T_N$ gradually decreases from 230 K ($x = 0$) to 185 K ($x = 0.5$). For $x \bullet 0.45$, a novel multiferroic phase thus appears below $T_N$ ($<T_C$), associated with the antiferromagnetic ordering of off-center $Mn^{4+}$ ions.

Spontaneous electric polarization, $P_S$, along the *c*-axis was clearly observed in the *P*-*E* hysteresis curve, as shown in Fig. 5(c). The measured $P_S$ value at 2 K is ~ 4.5 μC/cm$^2$ in a specimen with heavily-twinned tetragonal domains, suggesting the intrinsic $P_S$ value of 13.5 μC/cm$^2$ for a single domain. The values of $P_S$ and $T_C$ for $x = 0.5$ are almost comparable with those for $BaTiO_3$ ($P_S$ = 26 μC/cm$^2$ and $T_C$ = 406 K). Since there are no lone pairs in $Sr^{2+}$/$Ba^{2+}$ ions, the observed ferroelectricity is attributed to the displacement of the magnetic $Mn^{4+}$ ion with $d^0$ configuration.

To further investigate the atomic displacements in the ferroelectric lattice for x = 0.5, we performed the single-crystal structural analysis by using synchrotron X-ray diffraction at BL-8A. Figures 6(a) and (b) show the detailed crystal structures at 225 K (above $T_N$) and at 50 K (below $T_N$), respectively. All the re•ection points are well assigned based on the non-centrosymmetric tetragonal *P*4*mm* space group at both temperatures. Note that the magnitude of shift of the $Mn^{4+}$ ion from the center of the surrounding oxygens is dramatically suppressed below $T_N$. In particular, the Mn-O-Mn bond significantly deviates from 180° above $T_N$ [~175.4(5)°], but becomes close to 180° below $T_N$ [~179.1(5)°]. This manifests itself as a huge change in tetragonality (*c*/*a*) by about 70% at $T_N$ (not shown here).

The mechanism of such strong suppression of tetragonality and/or ferroelectricity driven by the antiferromagnetic order can be explained in terms of the energy gain from the superexchange interaction between $Mn^{4+}$ ions. Since the 180° MnO-Mn bond is energetically favored for the antiferromagnetic coupling,

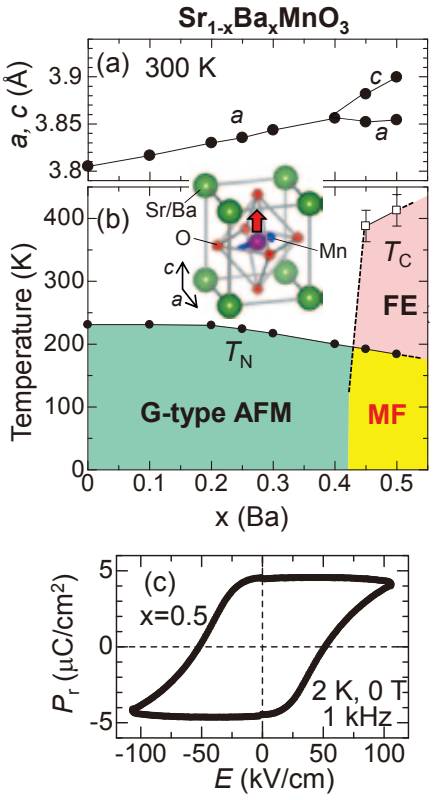


Fig. 5 (a) Lattice constant and (b) phase diagram for $Sr_{1-x}Ba_xMnO_3$ as a function of Ba concentration (*x*). PM, AFM, PE, FE, and MF denote paramagnetic, antiferromagnetic, paraelectric, ferroelectric and multiferroic phases, respectively. Inset: Crystal structure for tetragonal $Sr_{1-x}Ba_xMnO_3$. (c) Remnant P-E hysteresis curve for $x = 0.5$ along [001].

the positions of Mn and O ions shift so as to make the bond angle close to 180° (so-called inverse Kanamori-Goodenough rule) when the antiferromagnetic order (or fluctuation) occurs, resulting in suppression of the tetragonality. As for the variation of the spontaneous polarization $P_S$, assuming the relation $(c/a-1) \propto P_S^2$ which is valid for conventional ferroelectrics, the $P_S$ value above $T_N$ is estimated to be about twice as large as that below $T_N$; ~25 μC/cm$^2$ as a maximum. The antiferromagnetic ordering thus can produce huge variation in $P_S$ of the order of μC/cm$^2$.

Our results confirm the violation of the empirical "$d^0$-ness" rule for ferroelectric perovskites and open up a promising class of new multiferroic materials with large electric polarization and huge magnetoelectric coupling. These may be suitable for spintronics technology in the future.

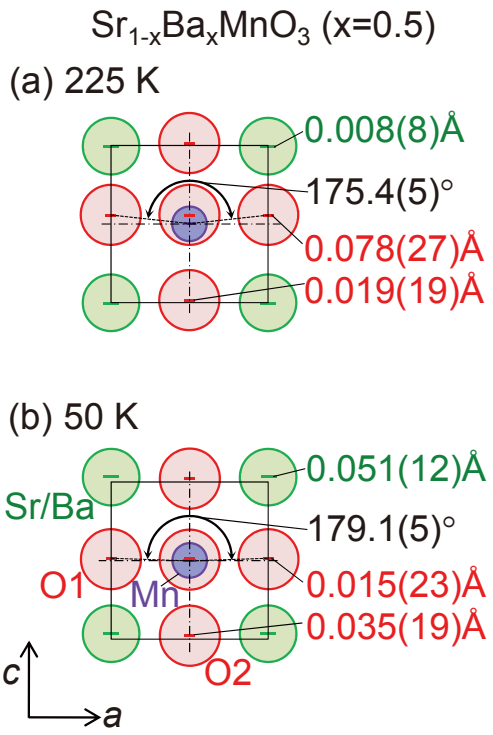


Fig. 6 Schematic diagrams of the crystal structure at (a) 225 K (above $T_N$) and (b) 50 K (below $T_N$), deduced from single-crystal X-ray diffraction. Each atomic displacement is shown on the basis of the Mn-centered unit cell.

**1-5 Pressure and randomness effects of spin-orbital order in $RVO_3$ [5,6]**

In $RVO_3$ ($R$: rare earth or Y), the two valence electrons of $V^{3+}$ ions occupy the near-triply degenerate $t_{2g}$ orbitals, and orbital and spin degrees of freedom exist. Hence, $RVO_3$ shows various physical properties owing to its orbital and spin states. Two types of spin-orbital ground state have been reported in the $RVO_3$ system. One is the phase with C-type orbital ordering (C-OO) and G-type spin ordering (G-SO). Here, C-type ordering means the antiferroic arrangement in the *ab*-plane and the ferroic arrangement along the *c*-axis, and G-type ordering means the antiferroic arrangement along the three principal cubic axes. The other ground state is G-type orbital ordering (G-OO) and C-type spin ordering (C-SO). The magnetic orderings of $V^{3+}$ ($S$ = 1) are dominated by the superexchange interaction depending on the orbital ordering, and the two spin-orbital ground states are expected to compete with each other energetically. We noted the "pressure effect" on the orbital states of $RVO_3$, and pressure-temperature phase diagrams for the orbital state have been investigated for $YVO_3$ and $TbVO_3$ [12], in which ground states are located near the boundary between the [G-SO,C-OO] and [C-SO,G-OO] phases. We clarified that the C-OO phase is significantly

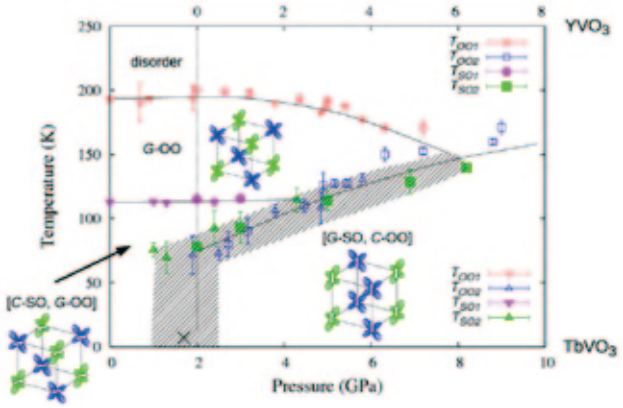


Fig. 7 Pressure-temperature phase diagram of the spin-orbital state for $YVO_3$ and $TbVO_3$. Circles and squares represent the phase-transition temperatures of $TbVO_3$, and triangles represent the phase-transition temperatures of $YVO_3$. The phase diagram of $YVO_3$ appears to be shifted as a whole to higher pressure by 2 GPa.

stabilized by the application of hydrostatic pressure in comparison with the G-OO one. However, the magnetic ordering has never been determined experimentally owing to the difficulty of doing so. Nevertheless, the magnetic state coupled with the orbital state is important in discussing the physical properties under high pressure.

In order to elucidate magnetic ordering under high pressure, neutron-diffraction experiments were performed using the thermal neutron spectrometer TOPAN, installed at the beam hole 6G of the JRR-3 reactor of JAEA, Tokai [5]. A hybrid anvil cell (HAC) was used for the neutron-diffraction experiments to obtain a high pressure of over 4 GPa [13]. We cut and shaped the samples such that they could be enclosed in the HAC; typical sample dimensions were 600x600x200 $\mu m^3$.

The magnetic phase diagrams for $RVO_3$ ($R$ = Y, Tb) were determined by low-temperature and high-pressure neutron diffraction techniques as shown in Fig. 7. We found that the magnetic ground state in $TbVO_3$ changes from C-SO to G-SO upon application of pressure. The transition of the magnetic ground state also indicates that the ground state of the orbital ordering changes from G-OO to C-OO. In $YVO_3$, the G-SO and C-OO phases set in simultaneously up to 6.2 GPa, and the disorder-[G-SO,C-OO] phase transition appears above 6 GPa. This is the first observation of a simultaneous spin and orbital order–disorder phase transition in perovskite-type transition-metal oxides $RMO_3$. The [G-SO,C-OO] phase is strongly stabilized with increasing pressure, and both the covalency effect and the superexchange interaction play roles in this stabilization.

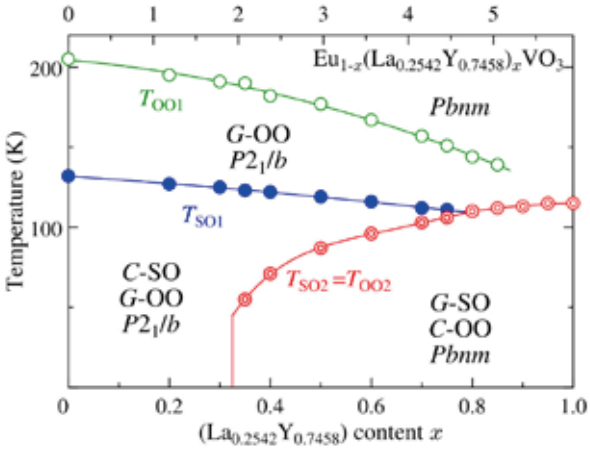


Fig. 8 Spin-orbital phase diagram of $Eu_{1-x}(La_{0.2542}Y_{0.7458})_xVO_3$. Open green, closed blue, and double red circles indicate the transition temperatures of the G-OO, C-SO, and [G-SO,C-OO], respectively. The top axis shows the variance of the ionic radius on the rare-earth site.

We also noted the "*R*-site randomness effect" of spin-orbital order in $RVO_3$ [6]. There, the effect was reported to be similar to the pressure effect. Therefore, we investigated the orbital-spin ordering in $Eu_{1-x}(La_{0.2542}Y_{0.7458})_xVO_3$ by complementary use of synchrotron X-rays and neutrons. There the average ionic radius of $(La_{0.2542}Y_{0.7458})^{3+}$ is the same as that of $Eu^{3+}$, and the variance linearly increases with x.

Finally, we determined the spin-orbital phase diagram of $Eu_{1-x}(La_{0.2542}Y_{0.7458})_xVO_3$ by using neutron scattering at TOPAN and resonant X-ray scattering at BL-4C, as shown in Fig. 8. By increasing randomness, G-OO and C-SO tend to be destabilized, while the other ordered phase is stabilized. This indicates that randomness acts as a parameter for stabilizing the [G-SO, C-OO] phase; this effect is the same as the pressure effect. The microscopic origins of the spin-orbital ordering, pressure and randomness effects are still open to question, and further theoretical studies are required.

[1] M. Uchida *et al.*, submitted.
[2] T. Toriyama et al., Phys. Rev. Lett. 107 (2011) 266402.
[3] A. Nakao et al., J. Phys. Soc. Jpn. **81** (2012) 054710.
[4] H. Sakai *et al.*, Phys. Rev. Lett. **107**, 137601 (2011).
[5] D. Bizen et al., J. Phys. Soc. Jpn. **81** (2012) 024715.
[6] R. Fukuta et al., Phys. Rev. B **84** (2011) 140409.
[7] C. T. Chen et al., Phys. Rev. Lett. **66,** 104 (1991).
[8] E. Pellegrin et al., Phys. Rev. B **53,** 10667 (1996).
[9] K. Hasegawa et al., Phys. Rev. Lett. 103 (2009) 146403.
[10] N. A. Hill, J. Phys. Chem. B **104**, 6694 (2000).
[11] S. Bhattacharjee *et al.*, Phys. Rev. Lett. **102**, 117602 (2009); J.M. Rondinelli *et al.*, Phys. Rev. B **79**, 205119 (2009); J.H. Lee *et al.*, Phys. Rev. Lett. **104**, 207204 (2010).
[12] D. Bizen et al., Phys. Rev. B **78** (2008) 224104.
[13] T. Osakabe et al., J. Phys. Soc. Jpn. **79** (2010) 034711.